Materials & Design 213 (2022) 110319

Contents lists available at ScienceDirect

Materials & Design

journal homepage: www.elsevier.com/locate/matdes

Interfacial adhesion strength of III-N heterostructures

Thomas Walter [a,*], Mohammad Zareghomsheh [a], Golta Khatibi [a], Vladimir N. Popok [b], Peter K. Kristensen [b], Ievgen Boturchuk [c], Sabine Schwarz [d]

[a] Christian Doppler Laboratory for Lifetime and Reliability of Interfaces in Complex Multi-Material Electronics, CTA, TU Wien, Getreidemarkt 9/164, 1060 Vienna, Austria
[b] Department of Materials and Production, Aalborg University, Skjernvej 4A, 9220 Aalborg, Denmark
[c] Center for Quantum Devices at Niels Bohr Institute, University of Copenhagen, Universitetsparken 5, 2100 Copenhagen, Denmark
[d] University Service Center for Transmission Electron Microscopy, TU Wien, Wiedner Hauptstraße 8-10, 1040 Vienna, Austria

HIGHLIGHTS

- The adhesion strength of AlN/Si as the weakest interface in an optoelectronic GaN based system is successfully determined for the first time.
- The interfacial fracture energy of the AlN/Si interface is strongly dependent on the layer design and microstructure yielding energy release rates between 2.8 J/m^2 and 13.6 J/m^2.
- Cross-sectional nanoindentation and four-point bending delamination tests revealed comparable local and large area interfacial fracture energy values.
- The probability of interfacial delamination or cohesive fracture in multilayers can be predicted by the proposed analytical model, allowing optimized thin film design.

GRAPHICAL ABSTRACT

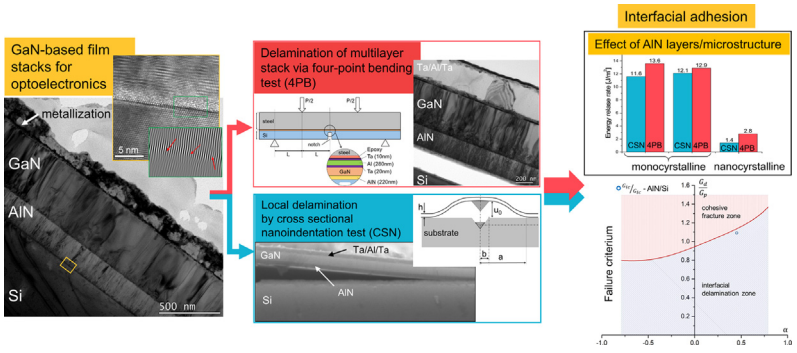

ARTICLE INFO

Article history:
Received 19 July 2021
Revised 9 December 2021
Accepted 9 December 2021
Available online 10 December 2021

Keywords:
III-N semiconductors
Thin films
Delamination
Nanoindentation
Fracture mechanics
HRTEM

ABSTRACT

Wide bandgap semiconductors such as group III-nitrides and SiC are considered as key materials for the fabrication of smaller, more reliable and efficient power electronics. Fabrication of robust and durable power devices requires an optimized design based on the understanding of the interfacial adhesion properties of the constituent thin-film heterostructures. In this study, the adhesion properties of GaN/AlN layers grown on Si substrates were investigated. Particularly, the influence of the AlN buffer layers, necessary for GaN growth on Si, on the delamination response was determined. The interfacial adhesion strength was obtained using cross-sectional nanoindentation (CSN) and four-point bending (4PB) tests. Analytical models based on beam- and elastic plate theory which were applied respectively to calculate the interfacial fracture energy (G_{ic}) for both methods are found to be in good agreement provided the loading conditions are similar. Detailed transmission and scanning electron microscopy investigations prior and subsequent to delamination reveal the microstructural details of the relevant interfaces and provide insights into the encountered mechanisms of interfacial failure. Finally, the probability of delamination along the weakest interface is discussed based on a fracture mechanics model.

* Corresponding author.
E-mail address: thomas.walter@tuwien.ac.at (T. Walter).

https://doi.org/10.1016/j.matdes.2021.110319
0264-1275/

Nomenclature

E	Young's modulus, [GPa]	P	load, [N]
G_{ic}	interfacial fracture energy, [J/m^2]	α	1st Dundur's parameter, [ ]
G_{IC}	fracture energy, [J/m^2]	β	2nd Dundur's parameter, [ ]
H	hardness, [GPa]	μ	shear modulus, [GPa]
h	thin film thickness, [m]	ν	Poisson's ratio, [ ]
I	moment of inertia, [kg/m^2]	σ_{yy}	tensile stress, [Pa]
K	stress intensity at a crack tip ($K_{I,II}$ are used for mode I and II), [MPa·m$^{1/2}$]	τ_{xy}	shear stress, [Pa]
		Ψ	mode mixity (phase) angle, [°]
K_{IC}	fracture toughness, [MPa·m$^{1/2}$]		

1. Introduction

Intensive research and development activities in recent years have demonstrated the great potential of GaN-based heterostructures for power, high-frequency and THz electronics [1-3]. GaN is typically grown on foreign substrates such as sapphire, silicon carbide and silicon. Although Al_2O_3 and SiC wafers exhibit the lowest lattice mismatch and difference in the coefficients of thermal expansion (CTE) with GaN [4], silicon is considered an important substrate for growth of the III-N heterostructures. Silicon wafers are inexpensive and available in large diameters with any necessary crystalline orientation, and using the existing Si-based production lines enables significantly lower manufacturing costs. However, direct growth of GaN on Si is a quite challenging task. The large lattice mismatch (~17 %) and difference in CTE (~54 %) of both materials lead to the formation of a high density of threading dislocations (TD) and cracking of the GaN films. Buffer layers consisting of AlN or AlN/AlGaN, with high thermal stability and good wettability to Si, have therefore been proposed to reduce the stresses and decrease the TD density [5]. In this case, Si (1 1 1) with a trigonal symmetry is often selected as the substrate material which favours an epitaxial growth of the wurtzite crystal structure of AlN [6].

The vapour pressure epitaxy method is most commonly used for AlN buffer layer growth. Controlling the state of compressive or tensile stresses during the processing is essential for an improved adhesion strength in GaN/Si wafers. However, the actual induced compressive stresses were often found to be insufficient due to the poor crystalline quality and the rough surface morphology of the AlN buffer layer [7]. Several approaches of tailoring the AlN layer design and fabrication process have therefore been proposed to counterbalance the effect of the tensile stress which develop during the cooling-down process [8]. To induce sufficient compressive stresses in the GaN, bilayer [9] or multilayer [10] AlN buffer designs with a mix of low- and high-temperature AlN or epitaxial lateral overgrowth using patterned Si substrates [6] have been applied. Even more it was found that the formation of an AlN layer with a high structural quality, which is mandatory for a good epitaxial GaN growth, can only be achieved at high temperatures of around 1100 °C [11]. Since the actual thin film structure strongly affects the state of internal stresses in the stack sophisticated experimental methods for determination of residual stresses have been suggested [12].

The structural, electrical and optical properties of GaN-based semiconductors have been investigated extensively [13]. However, studies on the interfacial adhesion properties of these structures are scarce. To our knowledge, though of high technological relevance, experimental value for the interfacial fracture energy (G_{ic}) of AlN/Si and AlN/GaN are not available.

From an experimental point of view, the external force or energy required to separate two adherent surfaces is the practical measure of interfacial adhesion. Using the fracture mechanics approach, the practical work of adhesion is measured by considering the interfacial fracture energy, the energy dissipated by the two materials during the separation, given as energy per unit area of the delaminated surface. This parameter is also commonly referred to as energy release rate in many publications [14]. Fracture toughness, interfacial fracture energy and crack growth rate in bi- and multilayer thin films can be determined using experimental data and analytical methods or finite-element simulations. The adhesion properties of thin films on brittle substrates can be characterized by a variety of nanoindentation techniques and beam bending tests. Four-point bending (4PB) has been widely used in the last few decades to study the mechanical properties of thin films, especially for interfacial adhesion measurement in microelectronics [15-17]. Recently, cross-sectional nanoindentation (CSN) is also utilized as a quantitative method to determine the nanomechanical properties of thin films grown on substrates for a wide range of materials. This method has been applied among others for the determination of the interfacial fracture energy (G_{ic}) of brittle dielectric/dielectric and metal/dielectric interfaces [18-22]. Microscopic examination of the delamination crack tip allows identification of the weak interfaces in the thin film stack.

Most of the available data on the adhesion properties of GaN-based semiconductors focus on the evaluation of the wafer bonding process [23,24]. In a study by Shi et al. [23], the adhesion quality of the wafer bonded GaN semiconductors was investigated using the double cantilever beam (DCB) test. It was shown that the high interface fracture energy of the bonded III-nitride wafers compared to the other III-V based semiconductors was due to the nature of their stronger chemical bonds. A reduction of the interface adhesion (bonding strength) to about 30–40% of the bulk fracture strength of the material was found to be caused by the high density of interfacial defects. These studies provide a good measure for the overall quality of the wafer bonds. However, the interfacial adhesion properties and the local delamination behaviour of these nanolayered thin films, even those of the well-known GaN/AlN structures have not been studied sufficiently.

In this study, the adhesion properties and delamination response of GaN/AlN films grown on Si substrates were investigated with respect to the influence of the AlN buffer layer.

Delamination experiments were carried out by the 4PB and CSN techniques and the interfacial fracture energy G_{ic} was calculated using the acquired data and appropriate analytical models. Applying these two methods allows to study the interfacial adhesion behaviour covering a length scale from a few micrometers to several millimeters. Microstructural examination of the interfacial features prior and subsequent to failure allowed interpretation of

the failure modes and mechanism of delamination in GaN/AlN layers grown on Si substrates.

2. Experimental procedures

2.1. Samples

The samples were commercial wafers with ~ 0.5 μm thick unintentionally n-doped GaN on Si (1 1 1) substrates by Kyma Inc. Two types of the AlN buffer (single and double layer) were formed by plasma vapour deposition on Si prior to the GaN film growth (see Table 1). Ti-based (Au/Ti/Al/Ti 60/30/90/30 nm) and Ta-based (Ta/Al/Ta 20/280/10 nm) stacks were formed on top of GaN in order to produce ohmic contacts. The structure and electrical properties of these metallization layers were investigated in an earlier publication [25].

2.2. Microstructural characterization

For the investigation of the microstructure and chemical composition of the thin film stacks as well as for determination of the crack path, TEM and scanning TEM (STEM) investigations combined with energy dispersive X-ray (EDX) analysis were performed using an FEI Tecnai F20 system. Images were undertaken on Dual-beam focused ion beam milled TEM lamellae of the cross-section of each sample type to study the interfaces of the stacks assisting the understanding of the fracture mode.

An FEI ESEM Quanta 200 system attached with an EDS Detector EDAX Genesis was used for chemical and microstructural analysis.

2.3. Mechanical and adhesion properties of thin films

Hardness and Young's modulus of the GaN and Si were determined by a nanoindentation method [26]. G_{ic} was obtained by means of quasi-static 4PB and CSN tests, as explained below.

2.3.1. Hardness test

The nanoindentation experiments were performed at 22.0 ± 0. 5 °C in a load-controlled manner with an ASMEC-Universal Nanomechanical Tester UNAT using a diamond Berkovich tip with a radius of 300 nm. Displacement and load noise level of the nanoindenter were below 0.5 nm and 3 μN, respectively. Before the test series, an indenter tip calibration was conducted in terms of indenter stiffness and contact area using fused silica and sapphire standards, according to the methods given by Oliver and Pharr [26]. During the testing, the indenter load was applied from both sides normal to the plane of the wafer surface. To measure the hardness of the GaN layer, the indenter depth was adjusted depending on the thickness of the metallization. A constant strain rate of 0.5 s^{-1} was kept throughout the tests. The load – displacement curves were obtained, and the Young's modulus, hardness, and plastic indent depth were extracted using the Oliver and Pharr method [26]. For the hardness and Young's modulus evaluation of the thin film coatings quasi-continuous stiffness measurement (QCSM) and cyclic-hardness measurements methods have been used [12]. Thermal drift and zero-point correction were performed automatically by means of the machine's software (Indent Analyser). To obtain an average value, the measurements were repeated 10 times with an indent distance of 50 to 60 μm to avoid elastic and plastic interactions. It is well known that possible pile-up and sink-in effects can alter the values of E and H measured by nanoindentation methods. Considering the indentation depth required and the absence of typical pile-up features in the indentation curves significant pile-up effects were not observed in our samples as confirmed by microscopic examination of the indented surfaces. Table 2 presents the Young's modulus (E) and hardness (H) values of the layers involved in the delamination process and includes also the literature data. As the thin AlN buffer layers, located between GaN and Si, were not accessible for the applied method, only literature values were used for all quantitative evaluations.

In the case of AlN films, a large variation in the literature data is observed, which is related to the deposition techniques, structure, layer thickness and substrate material. The reported E values vary between 243 and 342 GPa for nanostructured AlN films on Si (1 0 0) [29,30]. An increase of E from 270 to 342 GPa was found in [30] and explained by an increase in c-axis texturing in columnar nanostructured AlN films (~1μm) on Si (1 0 0) substrates. Significantly higher moduli of 390 GPa and H of 30 GPa for AlN films on c-plane sapphire, were reported for the films sputtered at 450 °C [31].

2.3.2. Four-point bending test (4PB)

4 PB tests, used for thin-film multi-layered stacks, were performed using sandwich structures, with the interfaces bonded face to face in the middle of the sample. At a certain bending moment, cracks, initiated at the pre-notch introduced in the centre of the substrate, propagated towards the thin film stack. Provided a sufficiently weak interface exists, the crack deflects outwards propagating along that interface. For steady-state crack growth, which is assured for a crack length large compared to the thickness of the layer system [32], G_{ic} becomes independent of the delaminated length. This allows calculation of the interfacial fracture energy by an analytical solution based on Euler-Bernoulli beam theory as a modification of Charalambides [15] according to

$$G_{ic-4PB} = \frac{P^2 L^2 (1 - \nu_2^2)}{8 E_2 b^2} \left(\frac{1}{I_2} - \frac{1}{I_c} \right) \quad (1)$$

where P is the load, L and b the distance between the inner and outer loading pins and width of the beam, respectively, and E_2 and ν_2 are the elastic modulus and Poison's ratio of the bulk substrate. The moments of inertia are calculated by

Table 1
Thickness of the III-N layers and substrates in the tested samples.

Film structure and layer thickness (μm)	GaN	AlN	AlN	Si
Ti-based stack/GaN/AlN/Si	0.45	0.2		400
Ta-based stack/GaN/AlN/Si	0.48	0.23		400
Ta-based stack/GaN/AlN-1/AlN-2/Si	0.47	0.22	0.2	400

Table 2
Hardness (H) and Young's modulus (E) of investigated materials.

Material	H [GPa]	E [GPa]	H [GPa] literature	E [GPa] literature
GaN	10.42 ± 0.06	274.9 ± 3	12–22[27]	287–320 [27]
Si (1 1 1)	10.1 ± 0.2	166.7 ± 4.2	12 [28]	188 [28]
AlN			12–22 [29,30]	243.5–342.3 [29,30]

$$I_2 = \frac{h_2^3}{12} \tag{2}$$

and

$$I_c = \frac{h_2^3}{3} + \lambda\frac{h_f^3}{3} + \mu\left(\frac{h_1^3}{3} + h_1^2 h_f + h_f^2 h_1\right) - \lambda\frac{[h_2^2 - \lambda h_f^2 - \mu(h_1^2 + 2h_f h_1)]^2}{4(h_2 + \lambda h_f + \mu h_1)} \tag{3}$$

where h represents the thickness with the subscripts 1, 2 and f referring to stiffener, substrate and thin-film multilayer using the following relations of the respective elastic moduli.

$$\lambda = \frac{E_f}{E_2}\frac{1-\nu_2^2}{1-\nu_f^2}, \mu = \frac{E_1}{E_2}\frac{1-\nu_2^2}{1-\nu_1^2} \tag{5}$$

As the analytical solution in this form only allows for a three-layer system, the elastic properties of the thin film stack were homogenized following linear beam theory according to [33].

Interpretation of the test results and determination of the cause and mechanisms of failure requires optical and chemical analysis of the delaminated surfaces. Though prevailing loading conditions at the crack tip require careful data analysis, the 4PB test is regarded as beneficial as it resembles operational loading conditions and provides stable crack propagation rates [16,17].

In this study, the 4PB investigations were performed by a micro tensile machine equipped with a bending module and a video microscope for in-situ monitoring of the crack opening and delamination growth. A sandwich-type sample design was realized by gluing a spring steel stiffener layer with a thickness of 700 μm on top of the metallization film stack. Prior to the testing, a notch was introduced in the middle of the specimen into the Si substrate using an abrasive wire saw. During the loading, an initial crack was generated at this location and propagated through the interface. For all tests, the distances between the inner loading pins and the outer supports of the 4PB jigs were 7 mm and 14 mm, respectively, with the radius of the support bearings being 1 mm. Displacement controlled loading was applied at a rate of 0.1 mm/min with load and transversal displacement monitored. More details on the applied 4PB method can be found in [34,35].

2.3.3. Cross-sectional nanoindentation

With CSN, an interfacial crack is initiated by indenting the tip into the cross-section of a brittle substrate close to the interface of interest, chipping of the substrate and separation of a wedge-shaped segment and the film from the body of the substrate. By increasing the indentation load, the separated layer is pushed away resulting in crack propagation in the interfacial region between the weakest interfaces [20]. CSN provides direct observation of the crack path in the cross-section of thin-film coatings. The interfacial fracture energy is determined either by means of the finite element method (FEM) [35,36] or is calculated analytically by:

$$G_{ic-CSN} = \frac{Eh^3 u_0^2 (1-\lambda)^4 (2F + \lambda F')}{12(a-b)^4} \tag{6}$$

where E and h are Young's modulus and thickness of the delaminated film respectively, a and b the geometric parameters of the crack (Fig. 1a), u_0 the wedge displacement and F, and $F' = \frac{\partial F}{\partial \lambda}$ being a function of $\lambda = b/a$ defined as:

$$F(\lambda) = \frac{2ln\lambda + \frac{1+\lambda}{1-\lambda}ln^2\lambda}{[(1+\lambda)ln\lambda + 2(1-\lambda)]^2} \tag{7}$$

As the delaminated stack consists of several layers, an effective Young's modulus for the film stack is calculated using a simple mixture formula:

$$E_{eff} = \mu_1 E_1 + \mu_2 E_2 \tag{8}$$

Several studies have shown that G_{ic} is highly dependent on the relative contributions of shear (τ_{xy}) and tensile (σ_{yy}) stresses occurring at the crack tip, which has to be considered when comparing quantitative results of different methods for delamination investigations. This mode-mixity can be mathematically described by the phase angle:

$$\Psi = tan^{-1}\left(\frac{\tau_{xy}}{\sigma_{yy}}\right) \tag{9}$$

which is found to remain constant at approximately 43° during 4PB steady-state crack growth [37], while it increases quickly from about 20° shortly after delamination onset, to a stable plateau around 48° for the CSN measurements [35,36].

For the CSN investigations, sample slips were mounted to a specifically designed sample holder and polished to obtain a surface roughness of below 20 nm, necessary to avoid any influence on the measurement results. The nanoindentation experiments were performed at 22.0 ± 0.5 °C in a load-controlled manner using a diamond Berkovich tip with a radius of 300 nm. Before the test series, an indenter tip calibration was conducted according to [26]. The optimum parameters to induce delamination were obtained by variation of the indentation force and distance (d) for a large number of tests. The onset of indentation delamination is observed at indentation loads between 80 mN and 120 mN at

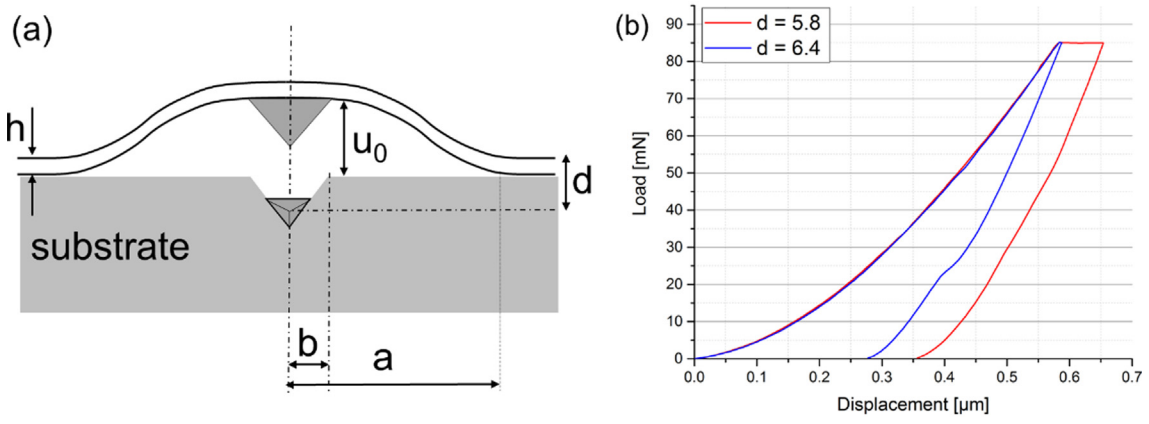

Fig. 1. (a) Schematic of the CSN test showing the geometrical relations needed for analytical calculation and (b) typical load–displacement curves obtained by CSN at various distances (d) to the surface of GaN samples with Ta-based stacks.

distances from the interface in the range of 1 to 7 μm. To avoid the interaction of the fractures, the distances between the indentations were set at 100 μm.

Fig. 1b shows typical load–displacement curves of CSN experiments obtained on GaN/AlN/Si samples at various distances (d) to the free surface at a load level of 85 mN. The critical load needed to initiate delamination, increases with the intent-interface distance (d), which can be seen when applying the load at different distances from the free surface. While at d = 5.8 μm the horizontal curve shape at maximum load indicates the occurrence of the interfacial delamination before the unloading step, the same load at d = 6.4 μm is insufficient to initiate cracking of the Si substrate and thus no visible delamination of the metallization is detected in the SEM analysis. By varying the distance d in combination with the indentation load, an ideal pair of values can be found for each sample ensuring maximum wedge displacement and thereby delamination, while still avoiding cracking or fracturing of the delaminated coating layers. After indenting, interfacial delamination areas were measured by optical and scanning electron microscopy (SEM). Together with the necessary geometric parameters (Fig. 1a) determined by SEM imaging of the CSN sites, G_{ic} is calculated according to the analytical solution in Eq. (6).

3. Results and discussion

3.1. Microstructure

The typical structure of the GaN/AlN/Si sample with a Ti-based film stack marked as metallization is presented in Fig. 2a. The cross-sectional TEM micrograph reveals the single AlN layer with a thickness of about 200 nm followed by the 450 nm thick GaN layer with a considerable number of dislocations in both the AlN and GaN layers. The HRTEM image of the GaN/AlN interface in Fig. 2b confirms the good epitaxial growth of the GaN layer with [0002] GaN || [0002] AlN. Images in Fig. 3a,b of the AlN/Si interface are viewed in the $[11\bar{2}0]$ AlN and $[\bar{1}10]$ Si projections, respectively. The single-crystalline AlN layer is found to grow on Si (111) with the crystallographic orientation relation: [111] Si || [0002] AlN and $[11\bar{2}]$ Si || $[\bar{1}100]$ AlN without any significant misalignment along the c-axis (Fig. 3c).

By performing a Fourier Transform (FT) of the HRTEM pattern (Fig. 3c), then selecting several calculated diffraction spots, and subsequent inverse FT, several stacking faults and dislocations could be identified near the AlN/Si interface. The generated stacking faults, which are emphasized with red arrows in the filtered image of the HRTEM micrographs (Fig. 3d), contribute to the relaxation of large interfacial strains between AlN and the substrate [38].

Detailed microstructural analysis based on HRTEM investigations of the samples consisting of two AlN buffer layers is described in the next section.

3.2. Adhesion properties

G_{ic} of the GaN/AlN/Si interfaces were determined subsequent to 4PB and CSN tests using the analytical methods described in section 2.3. In order to provide comparative quantitative values of G_{ic} for both test methods the influence of the loading conditions has to be minimized. Thus, only CSN delamination sites with a crack length above a sample dependent threshold with a similar mode-mixity ($\Psi = 48^{\circ}$) to that of 4PB ($\Psi = 43^{\circ}$) were considered for quantitative evaluation.

3.2.1. Four-point bending test results

Fig. 4a shows representative load–displacement curves obtained during the 4PB delamination tests for all three sample stacks. After a linear increase of the load, a first drop indicates the cracking of the substrate starting at the notch growing towards the film stack. The steel stiffener needed to inhibit vertical cracking of the whole sample, is bent elastically during testing. This results in a steady increase in the load during stable delamination growth which superimposes the typical load plateau caused by delamination. As we traced the crack tip using in situ optical microscopy the exact load levels corresponding to the steady-state crack propagation along the AlN/Si interface could be extracted and used as input parameters for the analytical calculations.

For all samples, initial crack growth occurs inside the Si substrate until it eventually reaches the interface with the AlN buffer layer at which point the delamination continues partially along the AlN/Si interface (Fig. 4b). Since both the Ti and Ta-based stacks are fabricated on halves of the same wafer, they show similar values for G_{ic} of 13.6 ± 2.7 and 12.9 ± 2.1 J/m^2 respectively (Table 3).

The fracture surfaces of the fully separated samples, which are shown in Fig. 5 and correspond to the images in Fig. 4b, reveal the cohesive cracking of the Si substrate at both sides of the notch

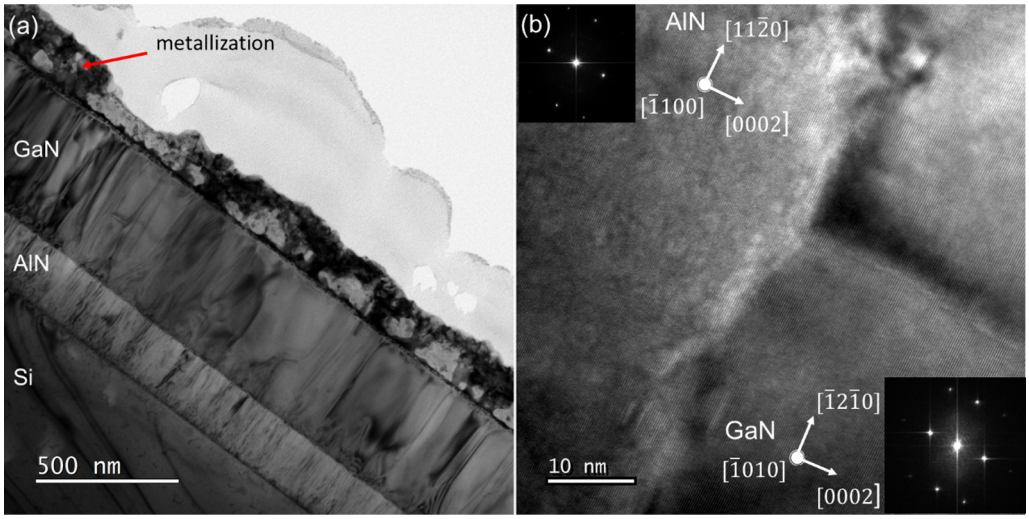

Fig. 2. (a) TEM micrograph of a Ti/GaN on Si sample reveals a layer composition and microstructure representative for both Ti and Ta metallized samples. (b) HRTEM image of the GaN/AlN interface shows the crystallographic orientation relationship.

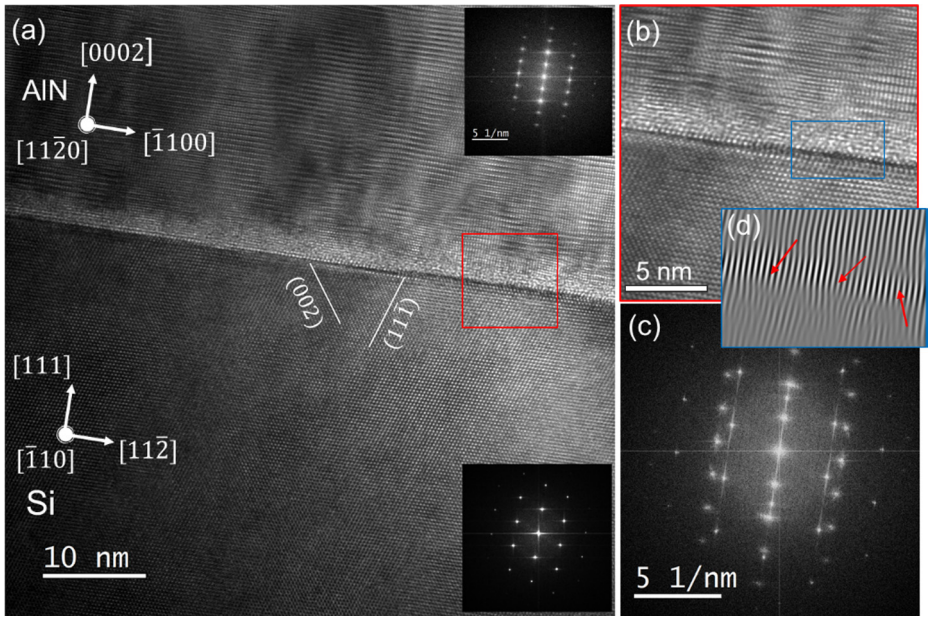

Fig. 3. (a) HRTEM image of the AlN/Si interface shows the crystallographic orientation relationship with (b) several stacking faults and dislocations in the AlN layer and (c) the corresponding diffraction pattern and (d) filtered image.

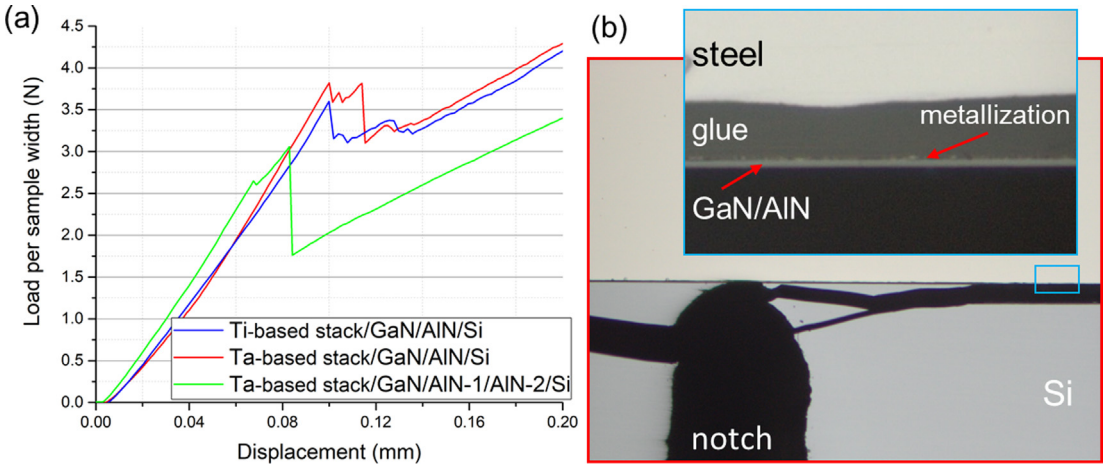

Fig. 4. (a) Load-displacement curves of the samples with Ta- and Ti-based metallization stacks as well as one and two AlN layers. (b) Optical microscope images showing the crack path inside the Si followed by delamination along the AlN/Si interface.

which eventually change the front and extend outwards along the AlN/Si interface as identified by EDX analysis (Fig. 5a,b). TEM and HRTEM images of a delaminated Ta-based stack/GaN/AlN/Si sample in the vicinity of the crack tip are presented in Fig. 6. The overlay of the elemental map shows the occurrence of delamination along the AlN/Si interface with a thin film of the Si substrate still partly attached to the AlN layer. Detailed images in Fig. 6b, c show the thickness and crystallographic orientation of the adhered Si film.

Table 3
Summary of calculated interfacial fracture energy (G_{ic}) of all samples.

Sample	Delaminated Interface	G_{ic}-CSN (J/m^2)	G_{ic}-4PB (J/m^2)
Ti-based stack/GaN/AlN/Si	AlN/Si	11.6 ± 2.6	13.6 ± 2.7*
Ta-based stack/GaN/AlN/Si	AlN/Si	12.1 ± 2.4	12.9 ± 2.1*
Ta-based stack/GaN/AlN-1/AlN-2/Si	AlN-2/Si	1.4 ± 0.7	2.8 ± 0.8
	AlN-1/AlN-2	2.6 ± 0.5	—

The samples with two buffer layers of AlN show similar behaviour with partial delamination along the AlN/Si interface. The significantly lower values of G_{ic} = 2.8 J/m^2 and the less pronounced cohesive cracking of the Si, indicates an inferior adhesion of the two-layered AlN films to the silicon substrate.

3.2.2. Cross-sectional nanoindentation test results

The SEM and TEM images of the delaminated samples are used to measure the geometrical parameters including the delamination length (a-b), wedge displacement (u_0) and intent-interface distance (d) for calculation of the G_{ic}. The interfacial fracture energy is calculated according to Eq. (6) after the determination of the geometric parameters from the SEM images of the CSN sites for all samples (Table 3). The G_{ic} value for the single-layered AlN/Si interface is found to be in the range of 11.6 to 12.1 J/m^2. The samples consisting of two AlN buffer layers show again considerably lower adhesion strength to the Si substrate with G_{ic} values of about 1.4 J/m^2 compared to the samples with one AlN layer. Additionally, in about

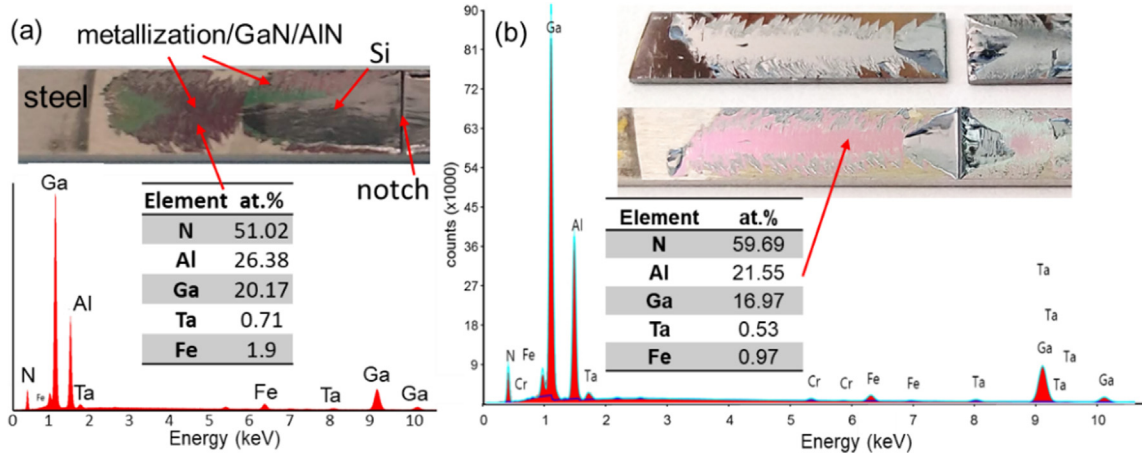

Fig. 5. (a) Image of the steel stiffener side revealing the leftovers of metals used for the top metallization and GaN as follows from EDX analysis (b) EDX and optical microscopy analysis of fully separated Ta-based GaN/AlN-1/AlN-2/Si samples revealing the crack path along the AlN/Si interface.

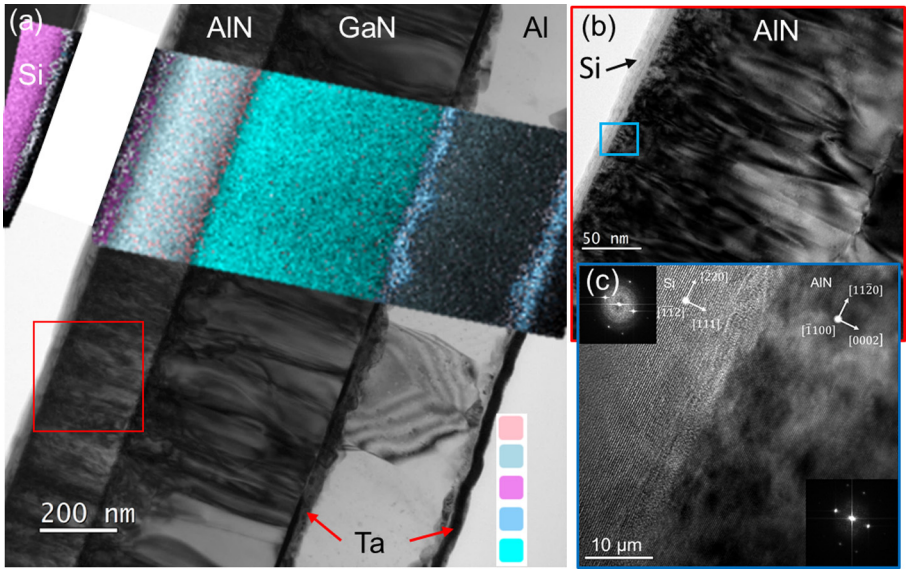

Fig. 6. Cross-sectional TEM images of Ta-based stack/GaN/AlN/Si sample revealing delamination along the Si/AlN interface as well as layers composition: (a) the entire heterostructure and metallization (b) AlN/Si interface and (c) high-resolution AlN/Si interface with FFT inserts.

20% of the cases, delamination appears along the AlN/AlN interface at similarly low values of about 2.6 J/m^2.

SEM images with EDX analysis of representative cross-sectional nanoindents of the Ti-based stack/GaN/AlN/Si and Ta-based stack/GaN/AlN/Si are presented in Fig. 7a and 7b,c respectively, showing clearly delamination along the AlN/Si interface. The delamination length is relatively short indicating good adhesion.

Delamination of the second type of GaN on Si, with two microstructurally different AlN buffer layers, also occurs predominantly along the AlN/Si interface. In this case the SEM images in Fig. 8a, b show a large delaminated area. The cracking along the AlN/Si is also confirmed by TEM images of FIB lamellas cut from the crack front of a CSN sample (Fig. 8c). Selected area electron diffraction patterns (SAED) in Fig. 8d and 8e reveal the monocrystalline and the nanocrystalline nature of the of AlN buffers below the GaN layer and above the Si substrate, respectively.

As mentioned above, in some cases the crack crossed through the first nano-crystalline AlN layer and followed the AlN/AlN interface further outwards as depicted in the SEM images with EDX line scan across the delamination site in Fig. 9.

The G_{ic} values of the two types of GaN/AlN/Si samples listed in Table 3 show a very good correlation between the CSN and 4PB methods. Comparative literature data for AlN/Si interfaces are not available, but the reported values for interfacial failure in brittle-brittle semiconductor systems are in the range from ~ 1 to about 14 J/m^2 [19,39-41]. The decrease of G_{ic} from 12 to 13.5 J/m^2 for the single-layered to ~ 1.4–2.8 J/m^2 for the double-layered samples suggests a strong impact of the structural features of the AlN buffer films on the overall adhesion of the system. In brittle multi-layered structures, where plasticity effects are absent or negligible, variation of the layer thickness and grain size mainly affect the state of internal stresses in the system. It has been reported that the adhesion strength of GaN-based semiconductors can be substantially improved by tailoring the order and thickness of AlN /AlGaN buffers and compensating internal stresses [6]. In a study on GaN-on-Si epitaxy, increasing the thickness of AlN buffer layer from about 200 to 400 nm resulted in a considerable reduction of the defect density and residual stresses due to the dominant state of compressive internal stresses [42]. The strong dependency of the interfacial strength on the film thickness was also reported

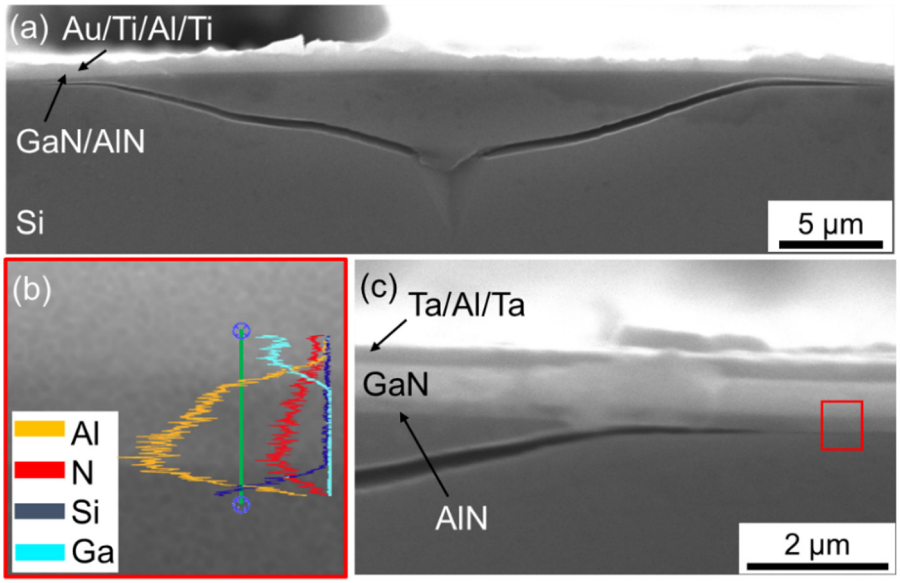

Fig. 7. SEM images of CSN delamination sites of the GaN on silicon samples with one buffer AlN layer showing the crack occurring exclusively along the Si/AlN interface: (a) Ti-based stack and (b, c) Ta-based stack.

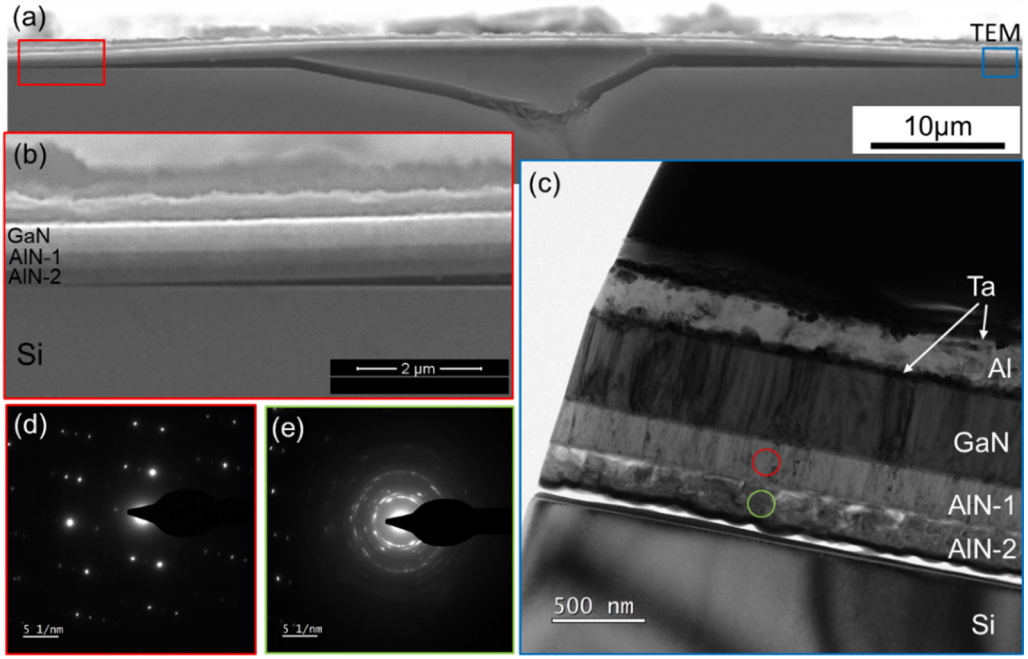

Fig. 8. (a, b) SEM micrographs of a delamination site after CSN of the two-layered AlN sample and (c) TEM image of a FIB lamella cut from the crack tip revealed the delamination along the AlN/Si interface. (d) SAED patterns of the first (aperture position marked by the red circle) and (e) second AlN layer (aperture position marked by the green circle) revealed the monocrystalline and nanocrystalline structure, respectively. (For interpretation of the references to colour in this figure legend, the reader is referred to the web version of this article.)

for GaN on sapphire bi-layers. It was found that a complete stress-induced self-separation of the GaN/sapphire interface can be achieved for a GaN layer thickness of 500–700 µm with a Gic of about 14 J/m^2 [40]. Though the processing conditions of the purchased wafers of the present study were not provided in details, the measured thickness of the monocrystalline and nanocrystalline AlN layers with a considerably different microstructure are both in the range of 0.2 – 0.23 µm. Since the CSN and 4PB delamination experiments show clearly the adverse effect of the additional 200 nm nanostructured AlN film, the lower interfacial fracture energy of the double-layered samples can be attributed to the higher amount of overall interfacial stresses in the stack, due to a higher structural incompatibility.

4. Fracture mechanics

According to our experimental results, the weakest site of the investigated metal/GaN/AlN/Si samples is found to be the interface between AlN and Si. In the following, we apply a fracture mechanics-based model first proposed in [42], which is adapted to the geometrical conditions of the CSN test and considers the

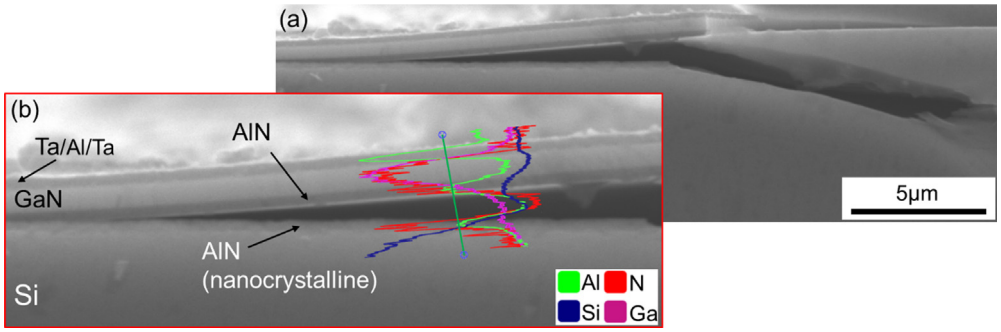

Fig. 9. (a) SEM images of delamination of the 2-layered AlN samples between the AlN layers as revealed by (b) EDX line scan across the crack depicted in the detail of the delamination front.

material properties of the bi-layer. For this purpose, the interfacial fracture energy for the deflection of a crack along the interface is compared with the fracture energy for the cohesive cracking of AlN.

Generally, a growing crack approaching and intersecting the interface between two bonded semi-infinite dissimilar materials at an arbitrary angle may advance by either deflecting along, or penetrating through the interface. Interfacial delamination in a bi-material occurs when the condition

$$\frac{G_{ic}}{G_{Ic}} < \frac{G_d}{G_p} \tag{10}$$

where G_{ic} is the experimentally obtained interfacial fracture energy and G_{Ic} is the fracture energy of the material 1 is satisfied. G_p and G_d are the theoretically calculated interfacial fracture energy for the crack that is penetrating the interface and the crack that has deflected into the interface, respectively (Fig. 10).

The ratio of the interfacial fracture energy of the deflected crack to the fracture energy of the penetrating crack G_d/G_p can then be plotted as a function of the dimensionless material parameter α (Dundur's parameter) which is dependent on the Young's moduli of the bi-layer [44]. The obtained curve corresponds to a threshold function of the interfacial fracture energy ratio, below which the crack will more likely propagates along the interface, while G_{ic}/G_{Ic} ratios above the curve lead to a cohesive failure of the material 1.

For the case of delamination along the AlN/Si interface, the ratio of the interfacial fracture energies G_d/G_p and the Dundar's parameter are determined by calculations presented in appendix A, and using the results of the CSN experiments. The main crack path along the AlN/Si interface as well the geometric relations, including the ratio of delaminated length to wedge side length (a/l) and the angle between impinging crack and the interface crack (ω), are taken from the SEM images of the delaminated interfaces. The magnitude of the crack wedging force during the nanoindentation (p) is determined by using the model proposed in [45]. Based on the obtained parameters $a/l = 0.5$, $\omega = 25°$ and $p = 0.022$ N, the ratio of interfacial fracture energy of the deflected crack to the fracture energy of penetrating crack G_d/G_p is plotted as a function of α as presented in Fig. 11.

To estimate the fulfilment of Eq. (10) for AlN/Si, the fracture energy (G_{Ic}) of AlN is derived based on Eq. (11) as suggested in [41] and assuming the average values of E = 300 GPa and K_{Ic} of *1.7* MPa•m$^{1/2}$ for AlN [29-31]:

$$G_{Ic} = \frac{K_{Ic}^2}{E} \tag{11}$$

Considering the experimentally obtained G_{ic} = 11.85 J/m^2, an average ratio of $G_{ic}/G_{Ic} \sim 1.09$ is obtained as shown in Fig. 11.

The results suggest that with the given ratio of G_d/G_p and $\alpha \approx 0.43$ the condition for interfacial delamination of AlN from Si is principally satisfied, however by a narrow margin. A variation of the mechanical properties may cause a small shift in the predicted response. Considering the scale dependent mechanical properties [46], determination of the actual fracture toughness of

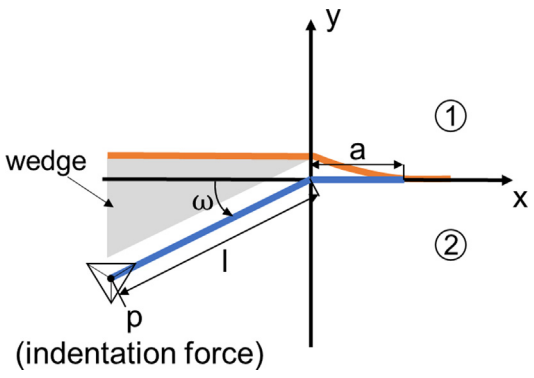

Fig. 10. Schematic drawing of an interfacial crack. A crack (l) which is initiated by the crack opening force (p) propagates through material 2 with the oblique angle (ω), is kinked at the interface and grows to a length of (a).

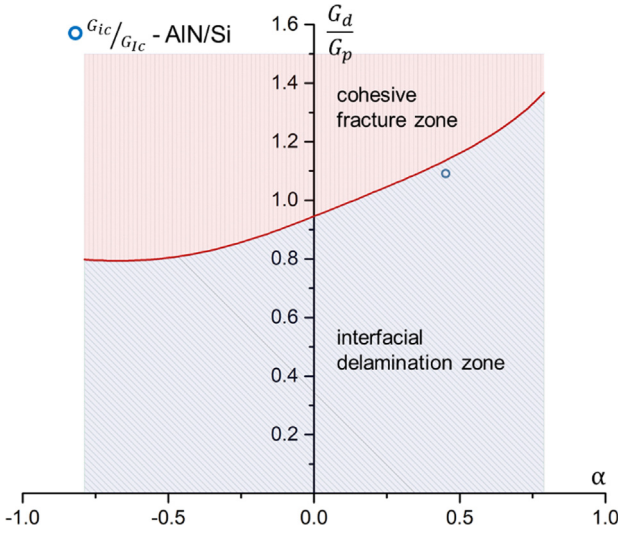

Fig. 11. Ratio of interfacial fracture energy of deflected crack to fracture energy of penetrating crack G_d/G_p for wedge loaded crack with $\omega = 25°$, $p = 0.022$ N, $a/l = 0.5$. The blue circle corresponds to the calculated G_{ic}/G_{Ic} ratio for delamination along the Si/AlN interface. (For interpretation of the references to colour in this figure legend, the reader is referred to the web version of this article.)

our ~ 200 nm AlN layers by applying suitable methods would provide an improved estimate. Nevertheless, due to the fact that in our experiments about 85% of the cracks resulted in full interfacial delamination between AlN and Si, the obtained results seem to be reasonable.

5. Conclusion

In this study, the adhesion properties of two types of GaN/AlN heterostructures grown on silicon substrates were investigated. These structures were specifically selected to investigate the effect of layer design and microstructure. The interfacial fracture energy of the samples consisting of a single and a double layer AlN buffer was measured using cross-sectional nanoindentation and four-point bending tests. The delamination experiments revealed AlN/Si to be the weakest interface. Quantitative evaluation yields similar results of both testing methods with G_{ic} of about 12–13.5 J/m^2 for the case of a single buffer layer. In the case of double-layer buffer structure, the presence of initial nanocrystalline AlN layer results in a strong drop of G_{ic} (1.4 J/m^2 by CSN and 2.8 J/m^2 by 4PB). The G_{ic} values confirm that introducing an AlN buffer layer with an optimized structure considerably improves the interfacial adhesion strength of the multilayered stacks.

A fracture-mechanics based model applied to the case of interfacial cracking induced by CSN in GaN/AlN/Si system confirmed the high susceptibility of the AlN/Si interface to delamination failure. The obtained results suggest that the model in combination with the CSN experiments can be successfully used to estimate the boundary conditions for cohesive or delamination failure in thin multilayer systems.

The findings of this study contribute to a better understanding of the adhesion properties of III–N semiconductors, which are of high technological relevance. Especially in the case of the GaN/AlN/Si stack, for which to our knowledge experimental values of the interfacial fracture energy were not available yet.

Declaration of Competing Interest

The authors declare that they have no known competing financial interests or personal relationships that could have appeared to influence the work reported in this paper.

Acknowledgement

The financial support by the Austrian Federal Ministry for Digital and Economic Affairs, the National Foundation for Research, Technology and Development (Austria) and the Innovation Fund Denmark (under project SEMPEL – Semiconductors for Power Electronics) is acknowledged. The authors acknowledge TU Wien Bibliothek for financial support through its Open Access Funding Programme.

Appendix A. .

An analytical model of indentation-induced stresses, based on linear elastic fracture mechanics, was used to estimate the thin film fracture toughness of a crack arising from the edge of a Berkovich indentation. The singular stress field analysis for the propagating crack approaching the interface was carried out by the methods proposed by He and Hutchinson (1989) [43] and Freund (1990) [47]. The crack is created by the crack opening force (p) and travels for a length (l) at an arbitrary angle (ω) towards an interface where it either penetrates the subsequent material or deflects along the interface for a length (a) (Fig. 10). For problems of this type, the solution variables of interest also depend on two dimensionless material parameters, i.e. Dundur's parameters α and β [45]. Considering the two materials being elastic and isotropic, α and β can be expressed by:

$$\alpha = \frac{\mu_1(1-\nu_2) - \mu_2(1-\nu_1)}{\mu_1(1-\nu_2) + \mu_2(1-\nu_1)} = \frac{\bar{E}_1 - \bar{E}_2}{\bar{E}_1 + \bar{E}_2} \tag{A.1}$$

and

$$\beta = \frac{1}{2}\left[\frac{\mu_1(1-2\nu_2) - \mu_2(1-2\nu_1)}{\mu_1(1-\nu_2) + \mu_2(1-\nu_1)}\right] \tag{A.2}$$

with μ, ν and $\bar{E} = E/(1-\nu^2)$ being the shear modulus, Poisson's ratio and the plane strain tensile modulus, respectively. As given in Table 2, the reported values for the Young's modulus of AlN vary in a rather broad range of 250 – 350 GPa. To consider this variation, an average of E = 300 GPa is assumed resulting in Dundur's parameters of $\alpha \approx 0.43$ and $\beta \approx 0.08$. Since the latter parameter is small compared to the former and only explicitly appears as β^2, it is commonly considered negligible [44].

The near tip stress field is in general induced by a combination of mode I and mode II loading, so that the complex interface stress intensity factor is calculated by $K = K_I + iK_{II}$. The solution for the stress intensity factors in the case of crack penetration is given in the model as

$$K_I + iK_{II} = c(\alpha, \omega, a/l) p l^{-\frac{1}{2}} \tag{A.3}$$

where c is a dimensionless complex-valued function, so, the interfacial fracture energy will be

$$G_p = \frac{1-\nu_1}{2\mu_1} |c(\alpha, \omega, a/l)|^2 \frac{p^2}{l} \tag{A.4}$$

In the case of crack deflection, the solution for the stress intensity factors is given by

$$K_I + iK_{II} = d(\alpha, \omega, a/l) p l^{-\frac{1}{2}} \tag{A.5}$$

yielding the following equation for the interfacial fracture energy.

$$G_d = \frac{1}{4}\left[\frac{1-\nu_1}{\mu_1} + \frac{1-\nu_2}{\mu_2}\right] \left|d(\alpha, \omega, \frac{a}{l})\right|^2 \frac{p^2}{l} \tag{A.6}$$

The ratio of the interfacial fracture energy is therefore

$$\frac{G_d}{G_p} = (1-\alpha)^{-1} \frac{\left|d(\alpha, \omega, \frac{a}{l})\right|^2}{\left|c(\alpha, \omega, \frac{a}{l})\right|^2} \tag{A.7}$$

Integral equation methods have been used to solve for the functions $c(\alpha, \omega, a/l)$ in the case of the penetrating crack and for $d(\alpha, \omega, a/l)$ in case of the deflected crack. The solution process for this problem finally leads to the following integral equations.

$$\int_{-1}^{1} \frac{\left(\bar{D}(x)\right)(1-u_2)}{(x-u_2)(1-x)} dx + \int_{-1}^{1} [D(x)G_1 + \bar{D}(x)G_2](1-x)^{-2} \exp(i\omega) dx +$$

$$+ \frac{1}{2}\int_{-1}^{1} [A(y)G_3 + \bar{A}(y)G_4] \exp(i\omega) dy = 0 \tag{A.8}$$

$$(1-\alpha)\int_{0}^{1} \frac{\bar{A}(y))}{(t_1 - y)} dy + \int_{-1}^{1} [D(x)F_1 + \bar{D}(x)F_2](1-x)^{-2} dx = 0 \tag{A.9}$$

in which $u_2 = (1-t_1)/(1+t_2)$ and

$$G_1(x, t_2) = \alpha \left[\frac{1}{z - \bar{z}_1} - \frac{\bar{z}_1 - z_1}{\left(\bar{z} - z_1\right)^2} + \frac{\bar{z}_1 - \bar{z}}{\left(z - \bar{z}_1\right)^2} \exp(2i\omega)\right] \tag{A.10}$$

$$G_2(x,t_2)=\alpha\left[\frac{1}{\bar{z}-z_1}-\frac{\bar{z}_1-\bar{z}_1}{\left(z-\bar{z}_1\right)^2}+\left(\frac{(z_1-\bar{z}_1)(z+\bar{z}_1-2\bar{z})}{\left(z-\bar{z}_1\right)^3}+\frac{1}{z-\bar{z}_1}\right)\exp(2i\omega)\right] \tag{A.11}$$

$$G_3(x,t_2)=(1-\alpha)\left[\frac{1}{z-y}-\frac{\bar{z}_1-\bar{z}}{(z-z_1)^2}\exp(2i\omega)\right] \tag{A.12}$$

$$G_4(x,t_2)=(1-\alpha)\left[\frac{1}{\bar{z}-y}-\frac{1}{z-y}\exp(2i\omega)\right] \tag{A.13}$$

$$F_1(y,t_1)=(1+\alpha)\left[\frac{1}{t_1-z_1}+\frac{\bar{z}_1-t_1}{(t_1-z_1)^2}\right] \tag{A.14}$$

$$F_2(y,t_1)=(1+\alpha)\left[\frac{1}{t_1-\bar{z}_1}+\frac{1}{t_1-z_1}\right] \tag{A.15}$$

with $z=t_2\exp i(\pi+\omega)$ and $z_1=\frac{1+x}{1-x}\exp i(\pi+\omega)$.

The complex-valued functions, D(x) and A(y), are constructed as following

$$D(x)=\left(\frac{(1-x)}{2}\right)^{\lambda}\left(\frac{(1+x)}{2}\right)^{-p}\left[C_0+(1-x)\sum_{k=1}^{n}d_kT_{k-1}(x)\right] \tag{A.16}$$

$$A(y)=y^{-p}(1-y)^{-0.5}\sum_{j=1}^{n}a_jy^{j-1} \tag{A.17}$$

where $T_k(x)$ is the Chebyshev polynomial of the first kind of degree k, and a_j and d_k are complex coefficients, which must be determined in the solution process. First of all, the complex constant C_0 is determined by the singularity analysis. By substituting equations (A.10) - (A.17) into the integral equations (A.8) and (A.9), the following two systems of algebraic equations can be obtained:

$$\sum_{k=1}^{m}\left[d_kE_{1k}(t_2)+\bar{d}_kF_{1k}(t_2)\right]+\sum_{j=1}^{n}\left[a_jG_{1j}(t_2)+\bar{a}_jH_{1j}(t_2)\right]+L_1(t_2,C_0)=0 \tag{A.18}$$

$$\sum_{k=1}^{m}\left\{d_kE_{2k}(t_1)+\bar{d}_kF_{2k}(t_1)\right\}+\sum_{j=1}^{n}\left\{a_jG_{2j}(t_1)+\bar{a}_jH_{2j}(t_1)\right\}+L_2(t_1,C_0)=0 \tag{A.19}$$

In general, they can be written as follows

$$\sum_{n=0}^{N}a_nG_n(t_i)=g(t_i)(i=0,1,\cdots.N) \tag{A.20}$$

These integrals, $G_{n(t_i)}$ and $g(t_i)$, are satisfied for any arbitrary values of t_i. Usually, for simplification, they are chosen as the roots of the Legendre or Chebyshev polynomials with a symmetric distribution with respect to the origin. The Gauss-Legendre quadrature rule was used to estimate the solutions of singular integral equations with m = n = 8 at 8 Gauss-Legendre points $\{t_i\}$ on the interval [-1, 1] for equation Eq. (A.18) and on the interval [0, 1] for Eq. (A.19). From Eq. (A.18) and. Eq. (A.19), 8 linear equations with 8 complex coefficients each are then obtained. Finally, by solving this system of linear equations, the 16 complex coefficients, d_k and a_j, can be calculated.

Data availability statement.

Derived data supporting the findings of this study are available from the corresponding author on request.

References

[1] J. Millan, P. Godignon, X. Perpina, A. Perez-Tomas, J. Rebollo, A survey of wide bandgap power semiconductor devices, IEEE Trans. Power Electron. 29 (5) (2014) 2155–2163, https://doi.org/10.1109/TPEL.2013.2268900.

[2] F. Zeng, J. An, G. Zhou, W. Li, H. Wang, T. Duan, L. Jiang, H. Yu, A comprehensive review of recent progress on GaN high electron mobility transistors: Devices, fabrication and reliability, Electron. 7 (12) (2018) 377, https://doi.org/10.3390/electronics7120377.

[3] K. Ahi, Review of GaN-based devices for terahertz operation, Opt. Eng. 56 (2017) 1. https://doi.org/10.1117/1.oe.56.9.090901.

[4] S.A. Kukushkin, A.V. Osipov, V.N. Bessolov, B.K. Medvedev, V.K. Nevolin, K.A. Tcarik, Substrates for epitaxy of gallium nitride: New materials and techniques, Rev. Adv. Mater. Sci. 17 (2008) 1–32.

[5] V.N. Popok, T.S. Aunsborg, R.H. Godiksen, P.K. Kristensen, R.R. Juluri, P. Caban, K. Pedersen, Structural characterization of MOVPE grown AlGaN/GaN for HEMT formation, Rev. Adv. Mater. Sci. 57 (2018) 72–81, https://doi.org/10.1515/rams-2018-0049.

[6] A. Krost, A. Dadgar, GaN-based optoelectronics on silicon substrates, Mater. Sci. Eng. B Solid-State Mater. Adv. Technol. 93 (1-3) (2002) 77–84, https://doi.org/10.1016/S0921-5107(02)00043-0.

[7] K.L. Lin, E.Y. Chang, Y.L. Hsiao, W.C. Huang, T. Li, D. Tweet, J.S. Maa, S.T. Hsu, C.T. Lee, Growth of GaN film on 150 mm Si (111) using multilayer AlN/AlGaN buffer by metal-organic vapor phase epitaxy method, Appl. Phys. Lett. 91 (2007) 2007–2009, https://doi.org/10.1063/1.2818675.

[8] S. Raghavan, J. Redwing, Growth stresses and cracking in GaN films on (111) Si grown by metalorganic chemical vapor deposition. II. Graded AlGaN buffer layers, J. Appl. Phys. 98 (2) (2005) 023515, https://doi.org/10.1063/1.1978992.

[9] Y. Lin, M. Yang, W. Wang, Z. Lin, J. Gao, G. Li, High-quality crack-free GaN epitaxial films grown on Si substrates by a two-step growth of AlN buffer layer, CrystEngComm. 18 (14) (2016) 2446–2454, https://doi.org/10.1039/C5CE02525G.

[10] K.-L. Lin, E.-Y. Chang, J.-C. Huang, W.-C. Huang, Y.-L. Hsiao, C.-H. Chiang, T. Li, D. Tweet, J.-S. Maa, S.-T. Hsu, MOVPE high quality GaN film grown on Si (111) substrates using a multilayer AlN buffer, Phys. Status Solidi Curr. Top. Solid State Phys. 5 (6) (2008) 1536–1538, https://doi.org/10.1002/(ISSN)1610-164210.1002/pssc.v5:610.1002/pssc.200778454.

[11] H. Marchand, L. Zhao, N. Zhang, B. Moran, R. Coffie, U.K. Mishra, J.S. Speck, S.P. DenBaars, J.A. Freitas, Metalorganic chemical vapor deposition of GaN on Si (111): Stress control and application to field-effect transistors, J. Appl. Phys. 89 (12) (2001) 7846–7851, https://doi.org/10.1063/1.1372160.

[12] M. Ghidelli, M. Sebastiani, C. Collet, R. Guillemet, Determination of the elastic moduli and residual stresses of freestanding Au-TiW bilayer thin films by nanoindentation, Materials & Design 106 (2016) 436–445, https://doi.org/10.1016/j.matdes.2016.06.003.

[13] V.F. Agekyan, E.V. Borisov, L.E. Vorobjev, G.A. Melentyev, H. Nykänen, L. Riuttanen, A.Y. Serov, S. Suihkonen, O. Svensk, N.G. Filisofov, V.A. Shalygin, L.A. Shelukhin, Optical and electrical properties of GaN: Si-based microstructures with a wide range of doping levels, Phys. Solid State. 57 (4) (2015) 787–793, https://doi.org/10.1134/S1063783415040046.

[14] W.W. Gerberich, M.J. Cordill, Physics of adhesion, Reports, Prog. Phys. 69 (7) (2006) 2157–2203, https://doi.org/10.1088/0034-4885/69/7/R03.

[15] P.G. Charalambides, H.C. Cao, J. Lund, A.G. Evans, Development of a test method for measuring the mixed mode fracture resistance of bimaterial interfaces, Mech. Mater. 8 (4) (1990) 269–283, https://doi.org/10.1016/0167-6636(90)90047-J.

[16] J. Chen, S.J. Bull, Approaches to investigate delamination and interfacial toughness in coated systems: An overview, J. Phys. D. Appl. Phys. 44 (2011) 1–35, https://doi.org/10.1088/0022-3727/44/3/034001.

[17] R.H. Dauskardt, M. Lane, Q. Ma, N. Krishna, Adhesion and debonding of multi-layer thin film structures, Eng. Fract. Mech. 61 (1) (1998) 141–162, https://doi.org/10.1016/S0013-7944(98)00052-6.

[18] J.M. Sánchez, S. El-Mansy, B. Sun, T. Scherban, N. Fang, D. Pantuso, W. Ford, M. R. Elizalde, J.M. Martínez-Esnaola, A. Martín-Meizoso, J. Gil-Sevillano, M. Fuentes, J. Maiz, Cross-sectional nanoindentation: a new technique for thin film interfacial adhesion characterization, Acta Mater. 47 (17) (1999) 4405–4413, https://doi.org/10.1016/S1359-6454(99)00254-2.

[19] T. Scherban, D. Pantuso, B. Sun, S. El-Mansy, J. Xu, M.R. Elizalde, J.M. Sánchez, J. M. Martínez-Esnaola, Characterization of interconnect interfacial adhesion by cross-sectional nanoindentation, Int. J. Fract. 120 (2003) 421–429. https://doi.org/10.1023/a:1024931913643.

[20] S. Roy, E. Darque-Ceretti, E. Felder, H. Monchoix, Cross-sectional nanoindentation for copper adhesion characterization in blanket and patterned interconnect structures: Experiments and three-dimensional FEM modeling, Int. J. Fract. 144 (1) (2007) 21–33, https://doi.org/10.1007/s10704-007-9072-7.

[21] X.J. Zheng, Y.C. Zhou, Investigation of an anisotropic plate model to evaluate the interface adhesion of thin film with cross-sectional nanoindentation method, Compos. Sci. Technol. 65 (9) (2005) 1382–1390, https://doi.org/10.1016/j.compscitech.2004.12.008.

[22] A. Roshanghias, G. Khatibi, R. Pelzer, J. Steinbrenner, On the effects of thickness on adhesion of TiW diffusion barrier coatings in silicon integrated circuits, Surf. Coatings Technol. 259 (2014) 386–392, https://doi.org/10.1016/j.surfcoat.2014.10.065.

[23] F.F. Shi, K.I. Chang, K.C. Hsieh, L. Guido, B. Hoke, Interface structure and adhesion of water-bonded GaN/GaN and GaN/AlGaN semiconductors, J. Appl. Phys. 95 (2004) 909–912, https://doi.org/10.1063/1.1633980.
[24] F.F. Shi, K.-L. Chang, K.C. Hsieh, Interfacial and mechanical characterization of wafer-bonded GaSb/amorphous α-(Ga, As)/GaAs structure for GaSb-on-insulator applications, J. Phys. D. Appl. Phys. 40 (24) (2007) 7694–7697, https://doi.org/10.1088/0022-3727/40/24/016.
[25] I. Boturchuk, T. Walter, B. Julsgaard, G. Khatibi, S. Schwarz, M. Stöger-Pollach, K. Pedersen, V.N. Popok, Structure and properties of Ta/Al/Ta and Ti/Al/Ti/Au multilayer metal stacks formed as ohmic contacts on n-GaN, J. Mater. Sci. Mater. Electron. 30 (19) (2019) 18144–18152, https://doi.org/10.1007/s10854-019-02167-2.
[26] W.C. Oliver, G.M. Pharr, An improved technique for determining hardness and elastic modulus using load and displacement sensing indentation experiments, J. Mater. Res. 7 (6) (1992) 1564–1583, https://doi.org/10.1557/JMR.1992.1564.
[27] C.-H. Tsai, S.-R. Jian, J.-Y. Juang, Berkovich nanoindentation and deformation mechanisms in GaN thin films, Appl. Surf. Sci. 254 (7) (2008) 1997–2002, https://doi.org/10.1016/j.apsusc.2007.08.022.
[28] A. Masolin, P.-O. Bouchard, R. Martini, M. Bernacki, Thermo-mechanical and fracture properties in single-crystal silicon, J. Mater. Sci. 48 (3) (2013) 979–988, https://doi.org/10.1007/s10853-012-6713-7.
[29] S.-R. Jian, J.-Y. Juang, Indentation-induced mechanical deformation behaviors of AlN thin films deposited on c -plane sapphire, J. Nanomater. 2012 (2012) 1–6, https://doi.org/10.1155/2012/914184.
[30] C. Besleaga, V. Dumitru, L.M. Trinca, A.C. Popa, C.C. Negrila, Ł. Kołodziejczyk, C. R. Luculescu, G.C. Ionescu, R.G. Ripeanu, A. Vladescu, G.E. Stan, Mechanical, corrosion and biological properties of room-temperature sputtered aluminum nitride films with dissimilar nanostructure, Nanomaterials. 7 (2017) 1–26, https://doi.org/10.3390/nano7110394.
[31] Y.-J. Chiu, C.-Y. Yen, M.-S. Chiang, G.-J. Chen, S.-R. Jian, C. Wang, H.-L. Kao, Mechanical properties and fracture toughness of AlN thin films deposited using helicon sputtering, Nanosci. Nanotechnol. Lett. 9 (4) (2017) 562–566, https://doi.org/10.1166/nnl.2017.2357.
[32] H.C. Cao, A.G. Evans, An experimental study of the fracture resistance of bimaterial interfaces, Mech. Mater. 7 (4) (1989) 295–304, https://doi.org/10.1016/0167-6636(89)90020-3.
[33] R. Schöngrundner, M.J. Cordill, G.A. Maier, H.-P. Gänser, Adhesion energy of printed circuit board materials using four-point-bending validated with finite element simulations, Microelectron. Reliab. 55 (11) (2015) 2382–2390, https://doi.org/10.1016/j.microrel.2015.06.055.
[34] T. Walter, G. Khatibi, A delamination study on metallization stacks of power semiconductors, IEEE, 2017, pp. 1–7. https://doi.org/10.23919/EMPC.2017.8346902.
[35] T. Walter, M. Zareghomsheh, G. Khatibi, H. Danninger, Adhesion Properties of Thin Film Multilayers : Comparison of Nanoindentation and Four-Point-Bending Techniques, Mater. Sci. Forrum 1016 (2021) 1561–1568, https://doi.org/10.4028/www.scientific.net/MSF.1016.1561.
[36] M.R. Elizalde, J.M. Sánchez, J.M. Martínez-Esnaola, D. Pantuso, T. Scherban, B. Sun, G. Xu, Interfacial fracture induced by cross-sectional nanoindentation in metal-ceramic thin film structures, Acta Mater. 51 (14) (2003) 4295–4305, https://doi.org/10.1016/S1359-6454(03)00256-8.
[37] A.A. Volinsky, N.R. Moody, W.W. Gerberich, Interfacial toughness measurements for thin films on substrates, Acta Mater. 50 (3) (2002) 441–466, https://doi.org/10.1016/S1359-6454(01)00354-8.
[38] K.Y. Zang, L.S. Wang, S.J. Chua, C.V. Thompson, Structural analysis of metalorganic chemical vapor deposited AlN nucleation layers on Si (111), J. Cryst. Growth. 268 (3-4) (2004) 515–520, https://doi.org/10.1016/j.jcrysgro.2004.04.083.
[39] Michael Lane, Reinhold H. Dauskardt, Anna Vainchtein, Huajian Gao, Plasticity contributions to interface adhesion in thin-film interconnect structures, J. Mater. Res. 15 (12) (2000) 2758–2769, https://doi.org/10.1557/JMR.2000.0395.
[40] Mengda Li, Yutian Cheng, Tongjun Yu, Jiejun Wu, Jinmi He, Nanliu Liu, Tong Han, Guoyi Zhang, Critical thickness of GaN film in controllable stress-induced self-separation for preparing native GaN substrates, Mater. Des. 180 (2019) 107985, https://doi.org/10.1016/j.matdes.2019.107985.
[41] Dong Liu, Stephen Fabes, Bo-Shiuan Li, Daniel Francis, Robert O. Ritchie, Martin Kuball, Characterization of the Interfacial Toughness in a Novel "GaN-on-Diamond" Material for High-Power RF Devices, ACS Appl. Electron. Mater. 1 (3) (2019) 354–369, https://doi.org/10.1021/acsaelm.8b0009110.1021/acsaelm.8b00091.s001.
[42] Andrea Severino, Ferdinando Iucolano, Impact of growth conditions on stress and quality of aluminum nitride (AlN) thin buffer layers, Phys. Status Solidi Basic Res. 253 (5) (2016) 801–808, https://doi.org/10.1002/pssb:201552638.
[43] He Ming-Yuan, John W. Hutchinson, Crack deflection at an interface between dissimilar elastic materials, Int. J. Solids Struct. 25 (9) (1989) 1053–1067, https://doi.org/10.1016/0020-7683(89)90021-8.
[44] J. Dundurs, Discussion: "Edge-Bonded Dissimilar Orthogonal Elastic Wedges Under Normal and Shear Loading" (Bogy, D. B., 1968, ASME J. Appl. Mech., 35, pp. 460–466), J. Appl. Mech. 36 (1969) 650–652. https://doi.org/10.1115/1.3564739
[45] Jae-il Jang, G.M. Pharr, Influence of indenter angle on cracking in Si and Ge during nanoindentation, Acta Mater. 56 (16) (2008) 4458–4469, https://doi.org/10.1016/j.actamat.2008.05.005.
[46] J. Ast, M. Ghidelli, K. Durst, M. Göken, M. Sebastiani, A.M. Korsunsky, A review of experimental approaches to fracture toughness evaluation at the micro-scale, Materials & Design 173 (2019) 107762, https://doi.org/10.1016/j.matdes.2019.107762.
[47] L.B. Freund, Dynamic Fracture Mechanics, Cambridge University Press, 1990, pp. 152–220, https://doi.org/10.1017/CBO9780511546761.